Advanced Functional Materials

ADVANCED FUNCTIONAL MATERIALS
www.afm-journal.de

RESEARCH ARTICLE OPEN ACCESS

Mechanical Programming of PEGDA-β-CD Polyrotaxane-Based Hydrogels via Host–Guest Molecular Recognition

Shiyi Chen[1] | Xudan Xing[2] | Haopu Su[3] | Dominik Voll[1] | Xiaohe Xu[1] | Jiafeng Wan[1] | Tongtong Cui[1] | Christian W. Schmitt[1,4] | Stefan Bräse[3,5] | Peng Li[2] | Patrick Théato[1,4]

[1]Institute for Chemical Technology and Polymer Chemistry (ITCP), Karlsruhe Institute of Technology (KIT), Karlsruhe, Germany | [2]Department of Anesthesiology, Sichuan Provincial People's Hospital, School of Medicine, University of Electronic Science and Technology of China, Chengdu, China | [3]Institute of Organic Chemistry (IOC), Karlsruhe Institute of Technology (KIT), Karlsruhe, Germany | [4]Soft Matter Synthesis Laboratory – Institute for Biological Interfaces III (IBG-3), Karlsruhe Institute of Technology (KIT), Eggenstein-Leopoldshafen, Germany | [5]Institute of Biological and Chemical Systems – Functional Molecular Systems (IBCS-FMS), Karlsruhe Institute of Technology (KIT), Eggenstein-Leopoldshafen, Germany

Correspondence: Patrick Théato (patrick.theato@kit.edu)

Received: 13 May 2026 | **Revised:** 27 July 2026 | **Accepted:** 12 August 2026

Keywords: drug delivery | hydrogels | mechanical programming | molecular recognition | polyrotaxanes | tissue engineering

ABSTRACT

Polyrotaxane-based hydrogels with mechanically interlocked structures offer unique opportunities for designing biomaterials with tunable mechanical properties in tissue engineering. However, the polyrotaxane structure based on poly(ethylene glycol) (PEG) and β-cyclodextrin (β-CD) is considered negligible in the aqueous phase, limiting its integration into well-defined hydrogel networks. Here, we report a series of hydrogels constructed from poly(ethylene glycol) diacrylate (PEGDA)-β-CD polyrotaxanes and gelatin (Gel), loaded with curcumin as a therapeutic model. We demonstrate that the increasing number of threaded β-CD units on PEGDA chains induced an evolution of gel microstructure from disordered porous to ordered laminar morphology, thereby transforming the mechanical behavior from highly elastic, low-dissipated (13.53%) to high-damping states (46.56%), accompanied by enhanced toughness and modulus. Notably, low threading density variants exhibited desirable elasticity and recovery suitable for skin wound dressings, while higher threading densities enabled mimicking of highly dissipative biological tissues. In vivo studies further demonstrated the excellent wound healing performance of these hydrogels, due to their suitable mechanical properties and anti-inflammatory properties. In summary, this study highlights the critical role of polyrotaxane threading density in coupling supramolecular structure with mechanical and biological functions, providing a versatile strategy for advanced tissue engineering materials.

1 | Introduction

Hydrogels are hydrophilic and porous 3D networks of crosslinked polymers swollen in water and play a vital role in tissue engineering (TE) [1]. They bridge the gap between physical and biological systems, often by mimicking the extracellular matrix (ECM), for their application in wound healing and tissue regeneration [2, 3]. In addition to the fundamental parameter of biocompatibility, the mechanical properties of hydrogels designed for TE should be tunable across a wide range to match native tissues

Shiyi Chen and Xudan Xing contributed equally to this work.

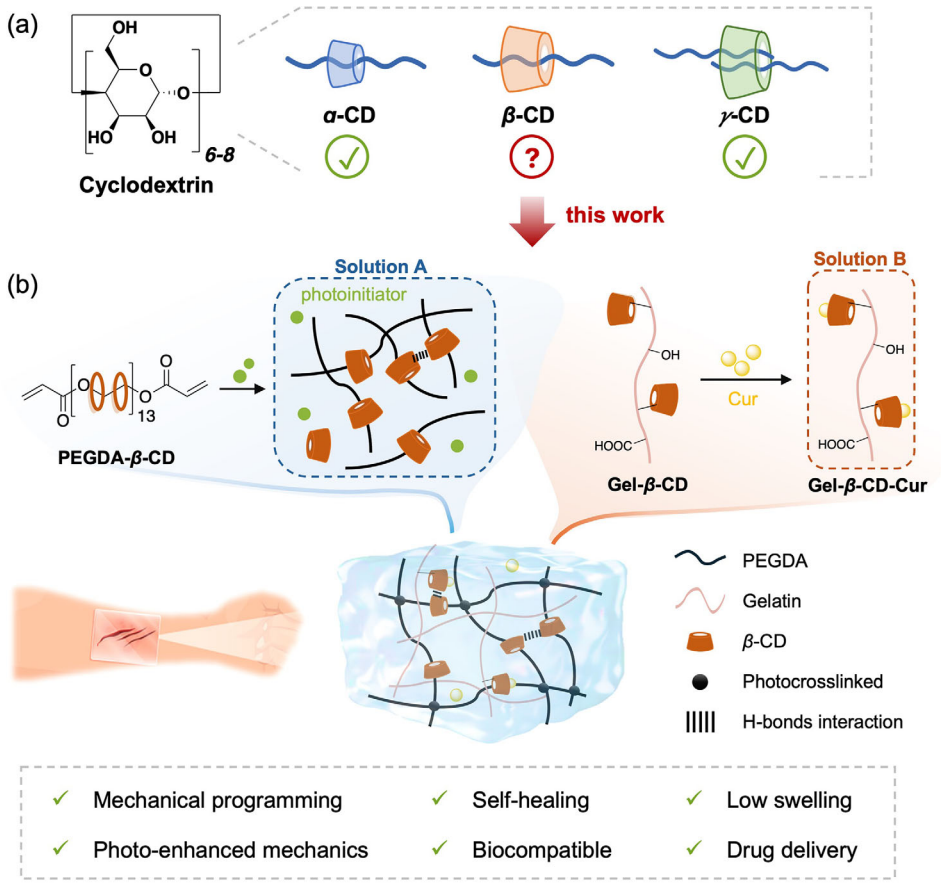

SCHEME 1 | (a) Pseudorotaxanes of different-sized cyclodextrins (α-, β-, and γ-CD) and PEG chains. (b) Illustration of the double network hydrogels $P_5C_{Z\text{-}H}GC_{10}$, comprising a photocrosslinked polyrotaxane structure and hydrophobic drug delivery functionality.

[4, 5]. At the cellular scale, cells sense and integrate mechanical signals by anchoring and pulling on their surroundings, thereby regulating important processes such as migration, proliferation, and differentiation [6, 7]. Meanwhile, wounds of different organs and tissues present distinct mechanical cues, including stiffness, viscoelasticity, and hydrodynamic force, which require hydrogels to exhibit mechanical compatibility [8]. Traditional hydrogels usually improve the stiffness simply by adjusting the concentration of precursors or increasing the crosslinking density, which is often accompanied by brittle fracture due to decreased toughness [9]. An alternative method is to construct specific topological structures, such as interpenetrating networks, mechanically interlocked structures, dense entanglements, or nanocrystalline domains [10]. Among them, polyrotaxanes (PRs), consisting of an axial molecule threaded through the cavities of one or multiple cyclic molecules, provide a unique mechanically interlocked topology that enhances mechanical performance while maintaining structural flexibility [11, 12]. In recent reviews, these design principles and emerging applications of such polyrotaxane-based networks and mechanically programmable biomaterials have been comprehensively described [13–15].

Cyclodextrins (CDs) are a class of cyclic oligosaccharides that consist of varying numbers of 6, 7, or 8 glucose units, which are named α-, β-, and γ-CD, respectively, and hence possess hydrophobic cavities with different diameters (Scheme 1a) [16]. Owing to their biocompatibility and ability for host–guest interactions, CDs have been widely used in drug delivery and mechanically interlocked systems. A polyrotaxane based on α-CD and poly(ethylene glycol) (PEG) host–guest system was first demonstrated by *Harada* and co-workers in 1992 [17]. Subsequently, α- and γ-CD were shown to form PRs with PEG derivatives due to their favorable cavity sizes: α-CD (4.7–5.3 Å) fit well and threaded tightly on the PEG chain with two C_2H_4O segments per CD ring, while γ-CD with a larger cavity (7.5–8.3 Å) can accommodate two PEG chains simultaneously, forming hydrogel networks [12, 18, 19]. In contrast, β-CD (6.0–6.5 Å) is often considered negligible due to its size mismatch with PEG chains, despite its advantages in cost, production scale, and biocompatibility [20, 21]. It has since been thought that β-CD can only form PRs with larger chains, such as polypropylene glycol (PPG) or aromatic-containing backbones [12, 22]. However, a first PR single-crystal structure of β-CD and PEG was reported by Udachin et al. [18] accommodating three C_2H_4O segments per CD. Yet, such an asymmetry situation between solid-state and aqueous environments limits its application as PRs in hydrogel systems.

At present, the molecular recognition between β-CD and PEG derivatives in low-concentration aqueous phases is still underexplored. Herein, we demonstrate that the β-CD hydrophobic cavity can recognize a short-chain PEG diacrylate (PEGDA) as an axial guest, through a well-defined threading to form a polypseudorotaxane PEGDA-β-CD in the aqueous solution. Definitive evidence

of its existence is provided by 1D and 2D NMR spectroscopy, while electrospray ionization mass spectrometry (ESI-MS) is used to analyze and evaluate the possible threading density. By virtue of the photocrosslinking properties of acrylate groups, PEGDA-β-CD (PC) with different threading densities is used as the first network in a hydrogel to provide structural support and mechanical programming. Meanwhile, the second network is mainly composed of β-CD-modified gelatin (Gel-β-CD, GC), which is orthogonally used to achieve hydrophobic drug loading and delivery. Finally, by interpenetrating these two networks at 5% PC and 10% GC, a kind of hydrogel $P_5C_{Z\text{-}H}GC_{10}$ ($PEGDA_{5\%}$-β-$CD_{Zero\text{-}High}$-Gelatin-β-$CD_{10\%}$) (Scheme 1b) is obtained, with tunable mechanics, self-healing property, low swelling, and high biocompatibility, which has potential applications in tissue engineering with on-demand design. In addition, curcumin (Cur) is selected as an unstable and water-insoluble drug model to evaluate the drug-loading capability of the newly developed gel matrix and further potential application as a wound dressing.

2 | Results and Discussion

2.1 | Host–Guest Recognition and Formation of Polypseudorotaxane PEGDA-β-CD

In pseudorotaxanes, β-CD inclusion complexes are typically obtained by mixing an aqueous solution of β-CD with guest molecules [23]. The formation of inclusion complexes is mainly attributed to weak host–guest interactions, resulting in small chemical shifts observable in the ^{1}H NMR spectra [24]. Based on this, we herein prepared aqueous solutions of PEGDA (700 Da) and β-CD at different molar ratios (1:1 to 1:10) in D_2O, and the resulting solutions were analyzed by ^{1}H NMR spectroscopy (Figure 1a,b and Figure S1). By comparing free β-CD and PEGDA-β-CD complexes, upfield shifts were observed for H3 and H5 protons of β-CD (Figure 1c), while all protons of β-CD showed a perceptible downfield shift with increasing β-CD ratio, especially the protons H2 and H4 on the outer side of the macrocyclic, due to changes in solvent viscosity, polarity, and de-shielding effect. However, the inner cavity protons H5 and H3 were most affected with a predominant upfield shift, confirming that the PEG chain was encapsulated as the guest molecule in the β-CD cavity.

The Rotating frame Overhauser Effect SpectroscopY (ROESY) was used for studying the interaction of CDs with guests, reflecting their spatial interactions [25]. Notably, several ROESY correlations appear at similar positions to those observed in the COrrelation SpectroscopY (COSY) spectra of the individual PEGDA and β-CD, which can be attributed to protons that are both J-coupled and spatially proximate. By comparing the ROESY spectra of PEGDA-β-CD (1:4) (Figure 1d) with the COSY spectra of the individual components (Figure S2), a clearly cross-ROE peak was observed between H1 at 5.07 ppm and H6 at 3.89 ppm, suggesting the formation of new spatial proximities induced by complexation. These observations suggested the presence of multiple β-CD units assembled along the PEGDA chain, which may bring different cyclodextrins into close spatial proximity.

However, due to the limited resolution of the 2D ROESY spectrum, 1D NOESY experiments were further conducted to investigate host–guest interaction with its higher sensitivity and resolution [26]. To investigate the interaction between the aliphatic PEGDA chain (protons b and c) and the inner cavity protons of β-CD (H3 and H5), selective 1D NOESY experiments were performed by irradiating individual resonances (Figure 1e). Upon selective irradiation of the proton at site c, clear NOE responses were observed for both H3 and H5, indicating close spatiality. Then, irradiation at site b resulted in NOE enhancement at H5. Additionally, selective excitation of H3 and H5 revealed that H3 showed NOE correlation with the proton at site c, whereas H5 exhibited correlations with both b and c sites on the PEGDA chain. These results collectively support the inclusion of the PEGDA chain within the β-CD cavity, with differential proximity of the guest protons along the chain to the inner cavity protons.

The inclusion complex PEGDA-β-CD (1:1–1:4) was characterized by Fourier transform infrared (FTIR) spectroscopy and compared with the physical mixture of PEGDA and β-CD (Figure 1f and Figure S3a). The overall signals of the inclusion complex were similar to those of free PEGDA and β-CD. However, blue shifts were observed in the C—H stretching vibrations of PEGDA (from 2866 to 2920 cm^{-1}) and the O—H stretching vibrations of β-CD (from 3270 to 3327 cm^{-1}) [27–29]. This may be due to the transition of guest long chains from a hydrated environment to a hydrophobic, spatially constrained microenvironment, which was not observed in the physical mixture. The physical mixture here referred to mixing equal amounts of PEGDA and β-CD precursors and testing immediately. To confirm the absence of inclusion behavior, the FTIR spectrum of the mixture was compared with the simulated FTIR spectrum of the mathematical summation of two precursors (Figure S3b). The differential IR spectrum of the mixture and the simulated one showed a very small fluctuation range ($\Delta A <\pm 0.05$), where the baseline close to 0 proved that the physical mixture had not yet formed a host guest interaction, exhibiting pure mathematical additivity.

After verifying the existence of PEGDA-β-CD polypseudorotaxane, the threading density was analyzed by electrospray ionization mass spectrometry (ESI-MS). This soft ionization should avoid the detachment of the β-CD from the polypseudorotaxane, in contrast to conventional chromatographic methods where its strong interactions with the silicon column surface may disrupt the host–guest interaction [30]. In the positive ion ESI-MS spectra (Figure S4), PEGDA (700 Da) exhibited a *Gaussian* distribution with the number of repeating units changing (n = 6 to 18), while β-CD displayed characteristic isotopic peak patterns [31, 32]. Various threading densities were found in PEGDA-β-CD inclusion complexes at different molar ratios (1:1–1:4), rising from one β-CD ring through one chain up to a structure of three β-CD rings through one chain (Figure 1g and Figures S5–S7). Based on these results, four types of PEGDA-β-CD ($PC_{Zero\text{-}High}$, with Zero, Z, 1:0; Low, L, 1:1; Medium, M, 1:2; High, H, 1:4 molar ratio) polypseudorotaxanes were identified and are in the following abbreviated as PC_Z, PC_L, PC_M, and PC_H. Their corresponding PEGDA:β-CD molar ratios, abbreviations, and possible interlocking structural derivatives from ESI-MS spectra are summarized in Table 1.

Subsequently, a series of P_xC_y hydrogels was prepared by adding x% (w.v., 2.5, 5, 10, 20%) of PEGDA and β-CD into H_2O at different molar ratios y (1:0–1:5). The gelation time upon photocrosslinking was studied systematically. As shown in Figure S8a,b, no gel

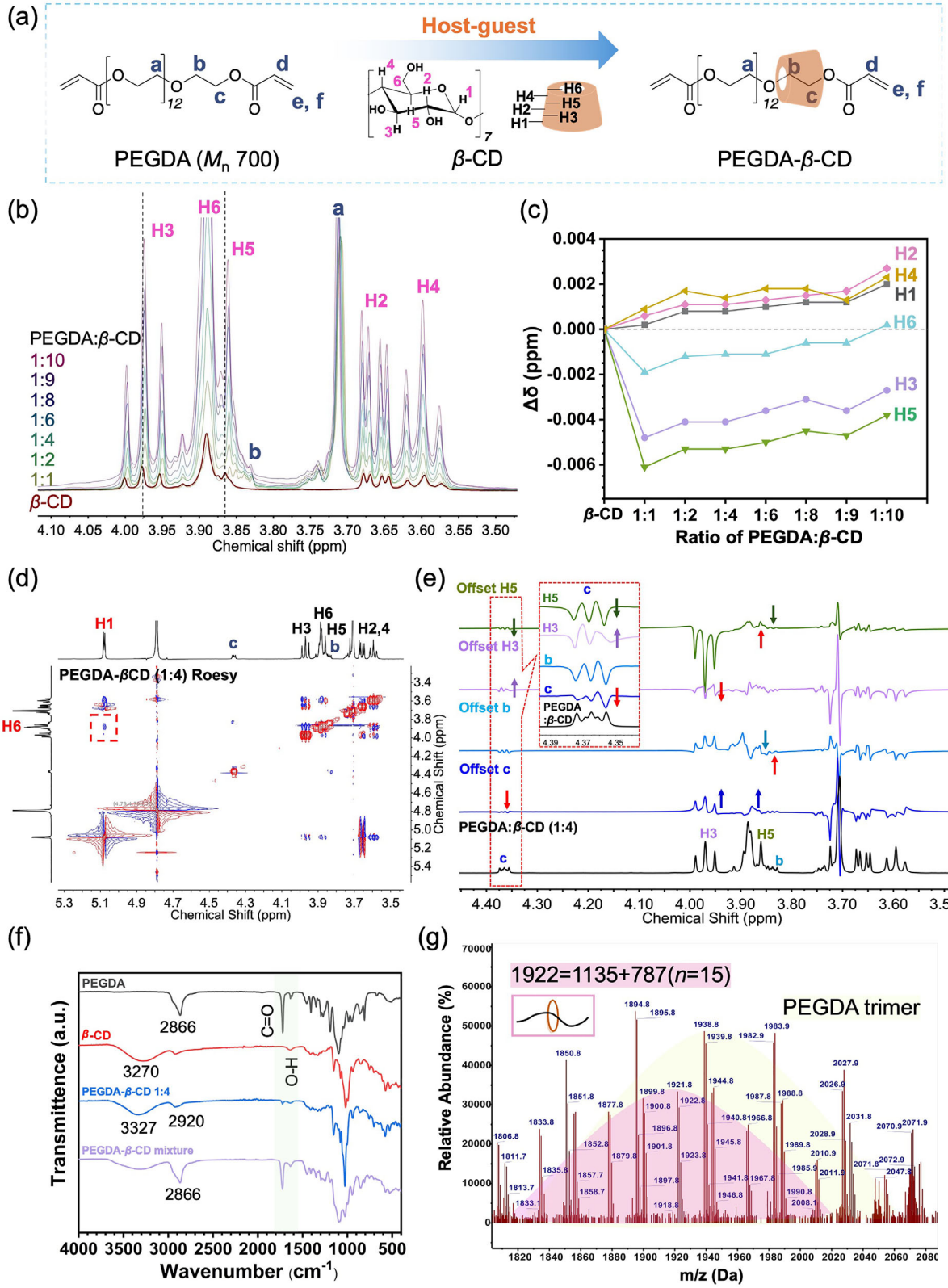

FIGURE 1 | (a) Formation of the pseudorotaxanes PEGDA-β-CD and numbering of a glucopyranose unit in β-CD. (b) ^{1}H NMR spectra of pure β-CD and PEGDA-β-CD inclusion complexes with different molar ratios (1:1-1:10) in D_2O at 298 K. (c) Chemical shift variations of β-CD protons in D_2O. (d) ROESY NMR spectrum of in D_2O of PEGDA-β-CD (1:4) in D_2O at 298 K, the red dashed boxes highlight ROE correlations of protons H1 and H6 on β-CD. (e) 1D selective gradient NOESY spectra (irradiated as highlighted with red arrows at protons c, b on PEGDA and H3, H5 on β-CD, respectively). (f) FTIR spectra of PEGDA, β-CD, PEGDA-β-CD (1:4) complexes, and physical mixture PEGDA+β-CD. (g) ESI-MS spectrum of PEGDA-β-CD (1:4) complex, showing PEGDA trimer and the complex structure where one β-CD ring is threaded onto the PEGDA short chain.

TABLE 1 | Four ratios of the PEGDA-β-CD polypseudorotaxane.

Molar ratio of PEGDA:β-CD	Classification	Abbr.	Possible interlocking structures
1:0	Zero (Z)	PC_Z	No polypseudorotaxanes
1:1	Low (L)	PC_L	
1:2	Medium (M)	PC_M	
1:4	High (H)	PC_H	

was formed in 30 min at extreme low concentration (2.5%) of PEGDA, while also a high ratio of β-CD would prevent gelation due to the steric hindrance of β-CD macrocycles, which hindered free radicals. By contrast, at 5/10% PEGDA ($P_{5/10}$), most mixtures formed gel states successfully within 30 min. To ensure that the interlocked β-CD would not dethread during photocrosslinking, $P_{5/10}C_{Z\text{-}H}$ hydrogel samples were selected after gelation under 30 min irradiation, followed by purification via dialysis against water. After 5 days of dialysis, any free β-CD was completely removed (Figure S9a–c). The remaining content of β-CD inside the network was determined using a phenol sulfuric acid colorimetric assay (Figure S10). Similarly, except for P_5C_H, all other ratios successfully formed gels, where the β-CD was found to be stably threaded inside the network, i.e., forming a polyrotaxane (Figure S9d,e). These results demonstrate that $P_{5/10}C_{Z\text{-}H}$ can serve as a stable first network for constructing polyrotaxane hydrogels.

2.2 | Preparation, Characterization and Drug Loading of Gel-β-CD

A second network was designed for drug loading that was composed of carboxymethyl-β-cyclodextrin (CM-β-CD) coupled to gelatin chains, which was achieved *via* *N*'-ethylcarbodiimide hydrochloride (EDC)/*N*-hydroxysuccinimide (NHS)-mediated coupling (Figure 2a and Figure S11a) [33, 34]. After 3 days of dialysis to completely remove ungrafted CM-β-CD (Figure S11b,c), the successful coupling was confirmed by ^{1}H NMR and FTIR spectroscopy. Figure 2b shows in the ^{1}H NMR spectrum the presence of both gelatin and CM-β-CD features in conjugated Gel-β-CD. Similarly, in the FTIR spectra (Figure 2c), Gel-β-CD displayed strong absorption bands related to two reactants, including amide I&II regions (1500–1700 cm^{-1}) from the gelatin skeleton and C—O—C stretching vibration (1000–1200 cm^{-1}) contributed by the ether group in CM-β-CD [35–37]. Moreover, the intensity of amide I&II in Gel-β-CD increased while the band of the carboxyl group (1590 cm^{-1}) from CM-β-CD disappeared, indicating the formation of new amide bonds. In contrast, the signatures of an FTIR spectrum of a physical mixture Gel+CM-β-CD remained unchanged. Since the amount of β-CD conjugated to the gelatin chains determines the drug-loading capacity, three different feed ratios (Gel: CM-β-CD, w/w, see Table S1 for details) were attempted. After complete dialysis to remove unreacted species, the CM-β-CD content in the final product was estimated by the absorbance at 490 nm of a phenol-sulfuric acid colorimetric assay (Figure 2d,e). The CM-β-CD contents obtained for the ratios of 3:2, 3:4, and 3:6 were 29.78 ± 2.67%, 34.57 ± 3.53%, and 44.37 ± 1.15%, respectively, which are consistent with previous reports [33].

Curcumin (Cur), as a hydrophobic drug, was loaded into Gel-β-CD and compared with PBS and pure Gel in terms of fluorescence intensity at around 530 nm (Figure S12c and Figure 2f,g). Cur exhibited negligible fluorescence in PBS due to its poor solubility in water, while its content in Gel-β-CD was about 7 times higher than that in pure Gel. Notably, the emission peak of Cur was around 538 nm, both in the curcumin fluorescence calibration curve (Figure S12a,b) and pure gelatin (Figure 2f) [38]. But it showed a significant blue shift (538–524 nm) after loading into the β-CD cavity, indicating the formation of the inclusion complex [16]. To maximize the drug loading potential, the highest CM-β-CD conjugation ratio (3:6) was selected for all subsequent experiments and defined as Gel-β-CD (GC), with the corresponding Cur-loaded was Gel-β-CD-Cur (GC-Cur).

2.3 | Design and Characterization of Polyrotaxane-Based Hydrogel $P_5C_{Z\text{-}H}GC_{10}$

For application in tissue engineering, which requires on-demand customization and inclusion of biological functions, $PC_{Z\text{-}H}$ with its polyrotaxane structure was used as the primary structural network, while Gel-β-CD (GC) served as the drug loading component. As a result, a series of hydrogels $P_5C_{Z\text{-}H}GC_{10}$ (Figure S13a) was synthesized in a water/glycerol binary solvent with 5% $PC_{Z\text{-}H}$ and 10% GC, ranging from $P_5C_ZGC_{10}$ without polyrotaxane to $P_5C_HGC_{10}$ with high threading density. Here, at the molecular level, the host–guest interactions served as structural templates for microstructural regulation. Scanning electron microscopy (SEM) images showed that the network changed from an isotropic disordered porous structure to an anisotropic laminar flow-like morphology (Figure 3a). This is because when an increased number of β-CD rings threaded onto the PEGDA chain, β-CD would arrange in a one-by-one arrangement on the chain, resulting in a high threading density. The hydrophilic outer layer of β-CD rings is rich in hydroxyl groups, which interact with other β-CD rings on adjacent PEGDA chains through hydrogen bonding, pulling the PEGDA chains closer and oriented. This indicated that the molecular recognition via host–guest interaction drove the topological evolution of the gel microstructure. Hence, such adjustable morphology of gels provides the possibility of adapting the mechanical properties to different organs and tissues.

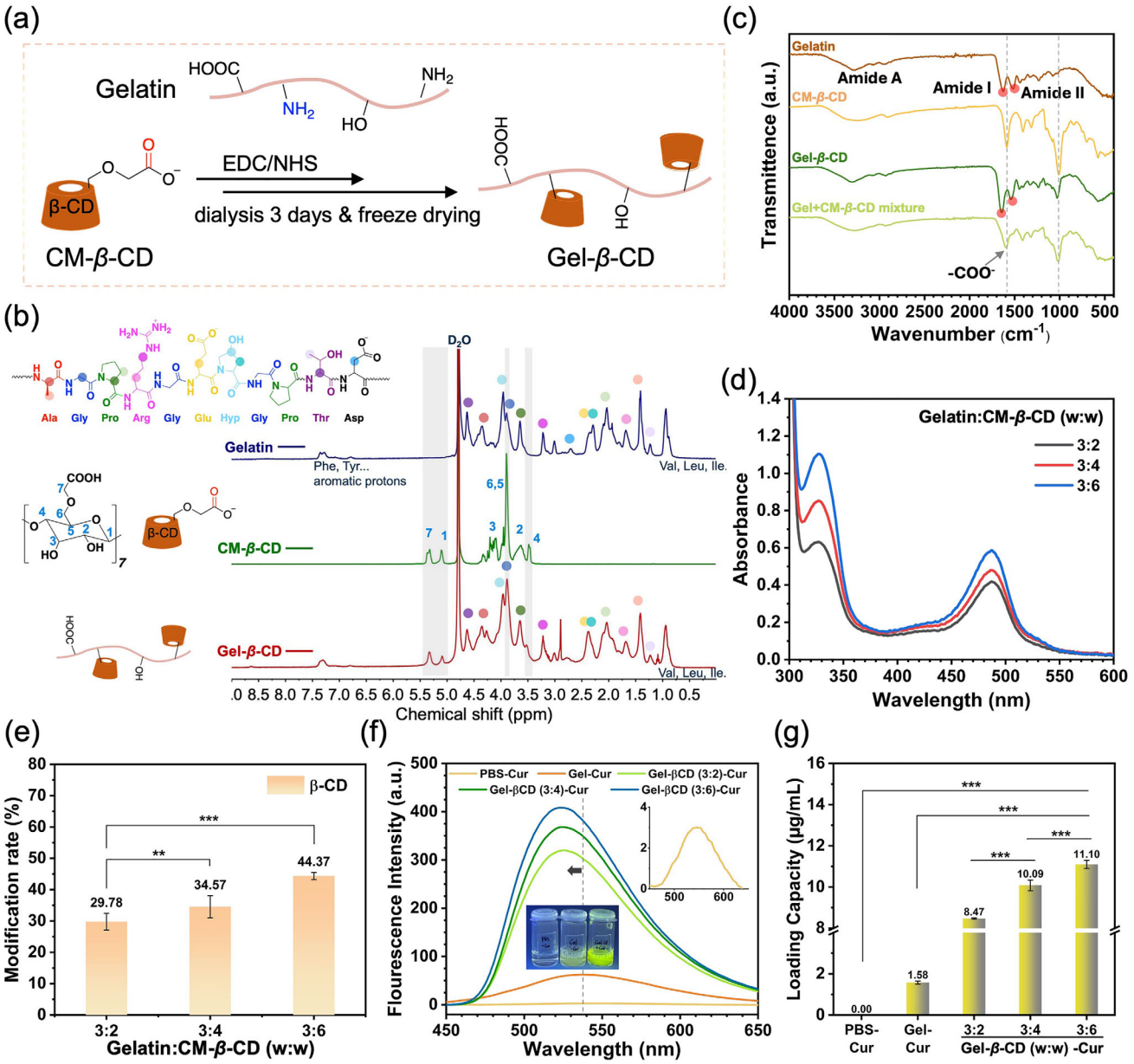

FIGURE 2 | Synthesis and characterization of Gel-β-CD for drug loading. (a) Synthesis route of Gel-β-CD. (b) ^{1}H NMR spectra of gelatin (Gel), CM-β-CD and Gel-β-CD in D_2O at 298 K. (c) FTIR spectra of gelatin (Gel), CM-β-CD, Gel-β-CD and physical mixture Gel+CM-β-CD. (d) UV–vis spectra of phenol-sulfuric acid colorimetric assay for Gel-β-CD at different feeding weight ratios. Peaks at 490 nm were used for estimation of (e) the modification rate of CM-β-CD on Gel-β-CD. (f) The emission spectra of PBS, Gel, Gel-β-CD loaded with curcumin, and the fluorescence intensities around 530 nm were used to calculate (g) the loading capacity of curcumin. In (e, g), data are presented as mean ± SD; $^*p < 0.05$, $^{**}p < 0.01$, $^{***}p < 0.001$, and ns denotes non-significant difference. $n = 3$ replicates.

Rheological tests were carried out on a series of hydrogels $P_5C_{Z\text{-}H}GC_{10}$ to analyze their viscoelasticity and self-healing ability. A dynamic strain sweep (DSS) test at a constant frequency of 1 Hz was first performed on $P_5C_LGC_{10}$ before and after UV irradiation to determine the mechanical enhancement during photo-crosslinking (Figure 3b). In the initial strain region, the storage modulus G′ was greater than the loss modulus G″ for both UV-irradiated and non-irradiated samples, showing the elasticity of the gel. After photo-crosslinking, both moduli increased slightly, and the crossover point (yield point, T_f) jumped from 26.71% to 138.34%, indicating that the photo-crosslinked network can bear more strain while maintaining intrinsic elasticity. Subsequently, the dynamic self-healing ability of $P_5C_LGC_{10}$ was confirmed through continuous-step strain measurement (Figure 3c). Under lower strain (1%), G′ was higher than G″, showing the integrity of the self-supporting network. Conversely, the values of modulus were reversed (G″> G′) under high strain (300%), demonstrating that the gel changed into the sol state with a flowing tendency. But once switching back to low strain (1%), G′ immediately raised again, greater than G″. In these cyclic tests, the gel showed instantaneous self-healing and recovery, which was attributed to abundant hydrogen bonding and supramolecular stacking between β-CDs on chains. In a “cut and heal” test (Figure 3d), $P_5C_LGC_{10}$ was able to self-heal after cutting and reconnection,

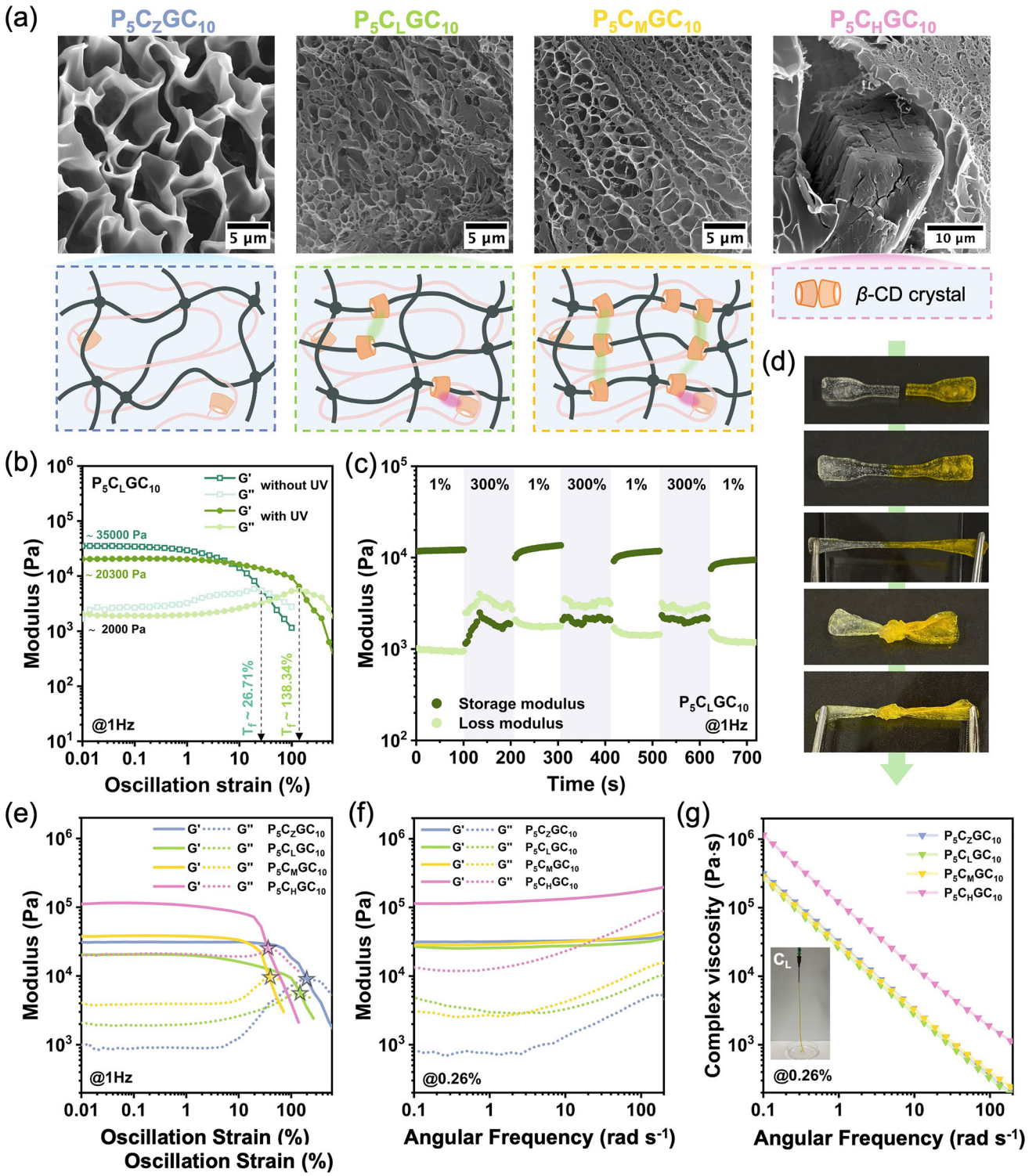

FIGURE 3 | Morphology and rheological characteristics of hydrogels. (a) SEM images showing morphology changes guided by molecular recognition, with schematic diagrams of the corresponding network. (b) Dynamic strain sweeps of $P_5C_LGC_{10}$ before and after photocrosslinking. (c) Continuous step-strain measurements of $P_5C_{Z\text{-}H}GC_{10}$ with high strain (300%) and low strain (1%) confirming self-healing ability. (d) Digital images of exhibiting self-healing behavior. Rheological behavior of (e) dynamic strain sweep, (f) dynamic frequency sweep, and (g) viscometry analysis for all formulations of $P_5C_{Z\text{-}H}GC_{10}$.

and did not break even when knotted or stretched. The comparison of FTIR spectra (Figure S14b) of $P_5C_LGC_{10}$ at different states (original, cutting, self-healing) showed a highly reversible transformation. The stretching vibration of the O—H group (3300 cm^{-1}) and the C—H group on the PEGDA skeleton (2800–3000 cm^{-1}) [28] showed slight shifts of 2–4 cm^{-1} after cutting. More interestingly, the amide II region at 1550 cm^{-1} disappeared after cutting and reappeared in the self-healed sample. The originally ignorable bands of restricted C—O—C glycosidic bridge from β-CD rings (1150 cm^{-1}) [39] were exposed after cutting, and significantly weakened again after healing.

Dynamic strain sweep (DSS) and dynamic frequency sweep (DFS) measurements were carried out on all hydrogel formulations of $P_5C_{Z\text{-}H}GC_{10}$ with different threading densities to explore their stability and differences. As shown in Figure 3e–g, $P_5C_HGC_{10}$ exhibited significantly higher G′ and complex viscosity compared to the other formulations, due to the presence of isolated β-CD crystals, as observed by SEM (Figure 3a). For all formulations in DSS, G″ was elevated with the increase of threading density caused by more dynamic interactions, such as β-CD sliding on the chains in polyrotaxanes and hydrogen bonding between each other [12]. However, the yield points of $P_5C_MGC_{10}$ and $P_5C_HGC_{10}$ were lower than those of $P_5C_{Z\text{-}L}GC_{10}$, which were consistent with the previous results of P_5C_H (Figure S8), as excessive β-CDs blocked partial photocrosslinking at low concentrations of PEGDA. Interestingly, in the initial strain stage, the G′ value of all formulations was one order of magnitude higher than G″, while the tan δ (G″/G′) was between 0.1 and 0.2, which resembled the characteristics of naturally occurring tissues, especially muscle and skin [8, 40]. In the DFS experiment of all samples (Figure 3f), the G′ consistently remained higher than G″ over a broad frequency range, indicative of a stable gel state. Meanwhile, the composite viscosity gradually decreased with increasing frequency, reflecting a shear-thinning effect caused by the alignment of polymer chains along the flow direction. Overall, these results demonstrated that $P_5C_{Z\text{-}H}GC_{10}$ gels possess tissue-like rheological properties and excellent self-healing ability.

2.4 | Mechanical Performance of Hydrogels $P_5C_{Z\text{-}H}GC_{10}$

To evaluate the mechanical adaptability of hydrogels $P_5C_{Z\text{-}H}GC_{10}$ in tissue engineering, the effect of polyrotaxane on mechanical properties was also studied through tensile and compression tests. First, the increase in threading density gradually enhanced the tensile strength, toughness, and elongation (Figure 4a,b and Figure S15). This improvement arose from the flexible mechanical interlocking of polyrotaxane, which is a topological constraint rather than a fixed chemical crosslinking. Because the host–guest interaction between the β-CD ring and PEGDA chain is dynamic and relatively weak, β-CD rings could move freely on the PEGDA chain as an axis, similarly to pulleys. Such *pulley effect* can equalize the tensions of threading polymer chains and avoid stress localization, thereby improving elongation and toughness [15]. Interestingly, after stretching and releasing, the four formulations exhibited different morphologies. Both $P_5C_ZGC_{10}$ and $P_5C_LGC_{10}$ showed full reversibility with no obvious deformation, whereas wrinkles appeared in $P_5C_MGC_{10}$, and $P_5C_HGC_{10}$ twisted into a helical shape (Figure 4c and Figure S16, Movie S1). This behavior was precisely regulated by the threading density at the molecular level and the different morphologies at the microscale level. When few or no β-CD rings were threaded onto the PEGDA chains, the gel could recover immediately after stretching and releasing, ignoring the strong interaction between β-CDs. Conversely, high threading density triggered hydrogen bonding interactions occurring between β-CD rings on adjacent chains (Figure 4c green). During stretching, the interactions would be disrupted and re-assembled with another β-CD ring in a new equilibrium position (Figure 4c red), preventing the macroscopic structure from reverting to its original state after release. The formation of wrinkles and helices can therefore be interpreted as morphological instabilities from a stress mismatch, caused by the breaking and recombination of non-covalent bonds in a polyrotaxane-based network [41, 42]. The cyclic loading-unloading tests (Figure 4d) were used to further explore the energy dissipation mechanism of dynamic bonds quantitatively. The dissipated energy per cycle is determined by the area of the hysteresis loop between loading and unloading, representing the actual amount of mechanical energy lost, which is converted into heat or used for molecular rearrangement [43].

Given the microstructural changes, $P_5C_ZGC_{10}$ and $P_5C_MGC_{10}$ were compared (Figure 4d). In the first cycle, pronounced hysteresis loops were observed on both formulations, mainly attributed to the Mullins effect, which states that the internal structure of the material is tamed during initial stretching [45]. The higher dissipated energy was observed in $P_5C_MGC_{10}$ than that in $P_5C_ZGC_{10}$ (Figure 4e), with an energy dissipation coefficient (η) close to 80% in the first cycle (Figure 4f), indicating that most of the mechanical energy during loading was effectively absorbed and converted. In the subsequent 9 cycles, the dissipation coefficients of $P_5C_ZGC_{10}$ and $P_5C_MGC_{10}$ quickly reached a stable plateau, representing rapid reconstruction after unloading and repeatable self-healing ability. Notably, $P_5C_ZGC_{10}$ displayed a stable, highly elastic, and reciprocating material, maintaining low energy dissipation (13.53 ± 1.41%). In contrast, $P_5C_MGC_{10}$ retained a high-energy dissipation coefficient (46.56 ± 3.00%), demonstrating its potential for damping application in TE. Leveraging its advantage, the samples with high threading density of polyrotaxane can serve as promising ECMs for tissue engineering where high energy dissipation is required [46]. For example, they could be utilized as treatments for cartilage or joint wound [47], shock-absorbing implants of plantar fat pads [48], or for noise suppression and vibration mitigation in wearable electronic devices, such as respiratory monitoring [49, 50].

Subsequently, as shown in Figure 4h,g, representative compression curves with corresponding modulus and strength revealed the different performances before and after irradiation. The result emerged in the enhanced compressive strength and modulus of $P_5C_LGC_{10}$ after photo-crosslinking, consistent with the previous rheological results (Figure 3b). A comparison of G_{10}, G_{10}-Gly, and hydrogels $P_5C_{Z\text{-}H}GC_{10}$ with four formulations exhibited a gradual improvement in compressive modulus (Figure 4i,j). Compared with traditional gelatin, which is fragile, all hydrogels showed compression resistance (Figure S17a) and maintained structural integrity even at strains exceeding 80%. Notably, $P_5C_HGC_{10}$ displayed a significantly higher compressive modulus, which is attributed to the formation of crystals within the network (Figure 3a). But the compressive strength of $P_5C_{M\text{-}H}GC_{10}$ was

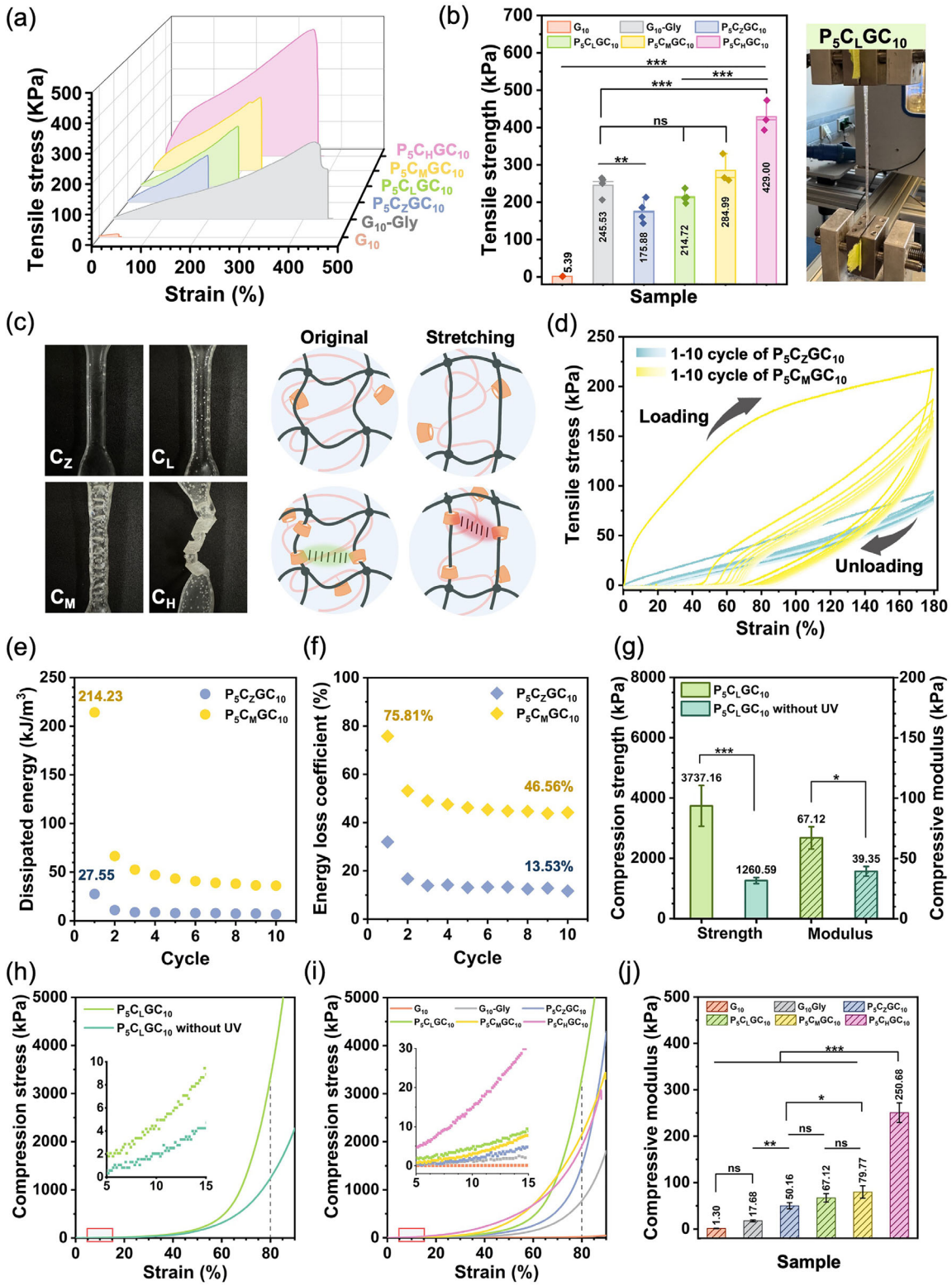

FIGURE 4 | Mechanical characterization of the hydrogels. (a) Tensile stress–strain curves of four formulations $P_5C_{Z\text{-}H}GC_{10}$, compared with G_{10} and G_{10}-Gly. (b) Ultimate strength obtained based on the corresponding tensile curve, and a digital image of the experimental setup with a stretchable sample. (c) Digital images of $P_5C_{Z\text{-}H}GC_{10}$ released after stretching to about 100% elongation, showing reversible morphology in $P_5C_{Z\text{-}L}GC_{10}$, with wrinkles appearing in $P_5C_MGC_{10}$, and helix structure in $P_5C_HGC_{10}$. (d) Cyclic loading-unloading curves with corresponding (e) dissipated energy and (f) energy loss coefficient (η) of the hydrogels $P_5C_ZGC_{10}$ and $P_5C_MGC_{10}$ during 10 cycles at 180% strain. (g) Compressive strength and modulus of $P_5C_ZGC_{10}$ before and after photocrosslinking, obtained from their (h) compressive stress-strain curves. (i) Representative compressive stress–strain curves and (j) compressive modulus of four formulations $P_5C_{Z\text{-}H}GC_{10}$ compared with G_{10} and G_{10}-Gly, which were calculated from the average slope of the stress-strain curve in the strain range of 5%–15% [44]. Data in (b, g, j) are presented as mean ± SD; $^*p < 0.05$, $^{**}p < 0.01$, $^{***}p < 0.001$, and ns denotes non-significant difference. $n = 3$ replicates.

lower than that of $P_5C_LGC_{10}$ because the photo-crosslinking was partially blocked (Figure S17b). The widely adjustable compression modulus of around 50–250 kPa is important for simulating tissues with different physiological stiffness. For example, the physiological stiffness range of dermal tissues is between 12 and 60 kPa [51], while cartilage and bone exhibit significantly higher stiffness (> 100 kPa) [52]. Accordingly, $P_5C_{Z\text{-}L}GC_{10}$ with its low modulus, high elasticity, reversibility, and low dissipation, is more inclined toward dynamic tissues such as skin. In contrast, gels with higher threading density, $P_5C_{M\text{-}H}GC_{10,}$ are better suited for simulating high-dissipating and stiffer tissues. All key mechanical parameters of samples are listed in Table S2.

2.5 | Physiochemical Adaptability and Drug Release of Hydrogels P5CZ-HGC10

The development of hydrogels suitable for tissue engineering also requires consideration of appropriate physiochemical properties, including adhesiveness, swelling ability, and degradability. The adhesive performance of hydrogels $P_5C_{Z\text{-}H}GC_{10}$ was evaluated through the lap-shear test (ASTM F2255) with porcine skin as the substrate, forming a sandwich structure with gels in between (Figure 5a and Figure S18). The adhesive properties of all samples were similar to previous hydrogel-based wound dressings, which can avoid pain during peeling [53], and slightly increased at body temperature (37°C), as the surface-modified Gel-β-CD still kept the inherent thermo-responsive behavior of gelatin. Further, all gels could adhere to finger joints comfortably, maintaining flexibility and complete adhesion even during finger movement (Figure 5b).

The swelling, water retention, and dynamic dehydration behavior of hydrogel $P_5C_{Z\text{-}H}GC_{10}$ was studied by gravimetric analysis. For wound healing, gels need to quickly absorb tissue fluid, and hence, most hydrogels will be highly swollen after absorbing fluid, resulting in expansion of the wound, potentially causing secondary damage [54]. Figure 5c shows that all four gels, $P_5C_{Z\text{-}H}GC_{10,}$ exhibited rapid liquid uptake within the initial 30 min due to the presence of hydrophilic glycerol and cyclodextrin. The final swelling ratio was only between 100% and 150%, which can be contributed to the short-chain PEGDA. In contrast, gels based on high molecular weight PEG (20 kDa) can swell up to 45 times [55]. Therefore, the PEGDA with low molecular weight (700 Da) limited the excessive expansion of the networks. Then, the gels swollen to equilibrium (i.e., after 2 h) were placed in an ambient environment to evaporate the free water until equilibrium, exploring the water retention capacity (Figure 5d and Figure S19b). The moisture content reached equilibrium after 10 h and remained almost unchanged for the next 14 days. Notably, the hydrogels with larger β-CD content maintained a higher equilibrium moisture content, which may be due to the hydrogen bond interaction between its rich peripheral hydroxyl groups and water molecules, thus effectively suppressing water evaporation. The main reason for the mass decline was that the glycerin in the gels was washed away during the swelling process and lost part of the water retention capacity. In fact, if the gels were only placed in an ambient environment without swelling, the samples containing glycerol remained flexible and elastic for at least 11 days, while pure gelatin without glycerol (G_{10}) became dry and brittle after one day (Figure 5e and Figure S19c, Movie S2). Overall, the hydrogels $P_5C_{Z\text{-}H}GC_{10}$ have the good properties of rapid absorption of tissue fluid, low swelling, and high moisture retention, which can be applied for long-term use.

As a representative hydrophobic drug, curcumin (Cur) was loaded into β-CD cavities in the network Gel-β-CD (GC) as previously proved in Section 2.2, then mixed with $P_5C_{Z\text{-}H}$ polyrotaxane to form the final drug-loaded hydrogels $P_5C_{Z\text{-}H}GC_{10}$-Cur (Figure S13a), and their release in vitro was monitored within 72 h. As shown in Figure 5f, a burst release behavior of Cur in G_{10} was observed within 8 h, while all formulations $P_5C_{Z\text{-}H}GC_{10}$-Cur provided a sustained and steady release profile over 72 h. This relied on Cur slowly detaching from the β-CD cavities, followed by its diffusion from the gel network into the surrounding medium. The capacity to maintain a drug concentration within wounds for an extended duration is beneficial for the repair of infectious wounds and avoids dosage toxicity [56]. To further understand the drug release mechanism, $P_5C_LGC_{10}$-Cur was picked as an example and fitted with three commonly used drug release models: zero order, first order, and *Higuchi* models (Figure 5g). The release pattern of the Cur in $P_5C_LGC_{10}$ was fitted to a first-order model (R^2 = 0.99), indicating that the release rate was primarily governed by the residual drug concentration within the matrix. Meanwhile, a relatively high correlation with the *Higuchi* model (R^2 = 0.95) suggested a dominant diffusion-controlled process, indicating that Cur was released more through diffusion from insoluble matrices rather than matrix erosion [57]. In order to further prove the universality of the hydrogel as a hydrophobic drug delivery platform, two widely used hydrophobic model drugs, berberine hydrochloride (BBH) and quercetin (QCT), were used to evaluate their loading and release performance (Figures S20 and S21). The abundant β-CD cavities in the Gel-β-CD could form host–guest complexes with the hydrophobic end of the drug, significantly increasing the loading capacity of BBH and QCT to 4.2 and 3.8 times that of pure gelatin, respectively (Table S3). In addition, $P_5C_LGC_{10}$-BBH/QCT, as the representative drug-loaded hydrogel, showed sustained release characteristics for both drugs within 72 h (Figures S20f and S21f). The release kinetics of BBH and QCT in $P_5C_LGC_{10}$ were similar to those of Cur, which fitted well to a first-order model, showing a concentration-dependent and diffusion-controlled process. These results together confirmed that the hydrogel can be used as a universal and efficient delivery platform for various hydrophobic drug therapies.

In addition, stable drug release is also governed by the structural integrity of the network and its appropriate degradation kinetics [58]. Meanwhile, biodegradation within a physiologically relevant timeframe is a prerequisite for tissue engineering biomaterials [59]. For this reason, the hydrogels were incubated in PBS (pH 7.4) or collagenase solution (2.5 U/mL) as a degradation medium at 37°C under constant oscillation to simulate *an* in vitro environment. The biodegradation of all samples was quantitatively assessed by measuring the mass loss at specific intervals of 3, 7, and 14 days, with Gel_{10} and Gel_{10}-Gly serving as control groups. As shown in Figure 5h, different from the rapid degradation of G_{10} and G_{10}-Gly, all formulations $P_5C_{Z\text{-}H}GC_{10}$ exhibited controlled degradation between 52% and 66% within 72 h, still maintaining certain structures. After 14 days, the gels degraded over 90%, which could be gradually replaced by newly generated tissue within an acceptable time range. Afterward, the enzymatic degradation of biomaterials was validated in a high-concentration

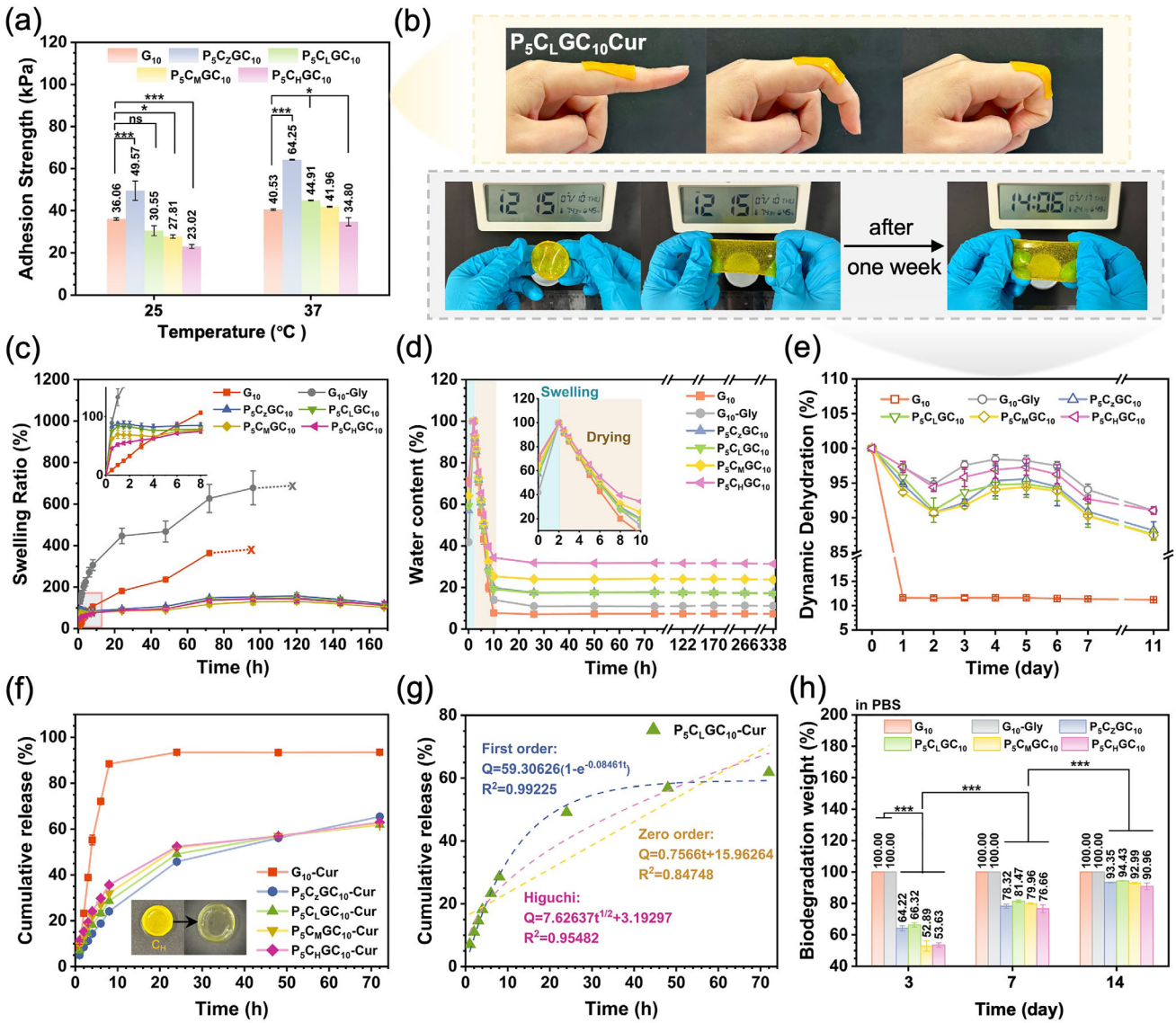

FIGURE 5 | Physiochemical adaptability and drug release of hydrogel $P_5C_{Z\text{-}H}GC_{10}$. (a) Adhesion strength of G_{10} and $P_5C_{Z\text{-}H}GC_{10}$ applied on porcine skin after 30 min of pressing at room temperature and 37°C. (b) Digital images of $P_5C_LGC_{10}$ as an example adhering to finger joints during movement. The behaviors of four formulations, $P_5C_{Z\text{-}H}GC_{10}$, compared with G_{10} and G_{10}-Gly, in (c) swelling tests, (d) water retention ability after swelling for 2 h, and (e) dynamic dehydration at room temperature for 11 days. (f) Curcumin release profile of G_{10} and $P_5C_{Z\text{-}H}GC_{10}$ in vitro over 72 h. (g) Evaluation of release mechanisms and kinetics of curcumin in $P_5C_LGC_{10}$ as a representative sample by fitting to zero-order, first-order, and *Higuchi* models. (h) Biodegradation behavior of G_{10}, G_{10}-Gly and $P_5C_{Z\text{-}H}GC_{10}$ in PBS at 37°C after 3, 7, 14 days. In (a, h), data are presented as mean ± SD; $^*p < 0.05$, $^{**}p < 0.01$, $^{***}p < 0.001$, and ns denotes non-significant difference. $n = 3$ replicates.

collagenase (2.5 U/mL in PBS) environment [60, 61], and the accelerated and complete degradation of all samples occurred within 3 days, demonstrating excellent enzymatic responsive biodegradability (Figure S19d).

2.6 | Evaluation of Cytocompatibility In Vitro and Wound Healing In Vivo

Excellent biocompatibility is a fundamental requirement for any material being used in TE applications. Therefore, the in vitro cytocompatibility of all drug-loaded hydrogels $P_5C_{Z\text{-}H}GC_{10}$-Cur was evaluated using cell counting kit-8 (CCK-8) assays in an indirect way and compared with gelatin (Figure 6a). Gelatin itself is highly advantageous for cell adhesion and growth due to the presence of the RGD peptide sequence, making it commonly used in TE [62, 63]. Notably, most samples in this study were outperformed by gelatin in terms of NIH/3T3 fibroblast activity. Among them, $P_5C_ZGC_{10}$-Cur showed significant differences, with 24-h cell viability reaching 175.5 ± 18.7%. This enhancement is likely due to the synergistic effect of the biocompatibility of polymer precursors and the anti-inflammatory property of loaded curcumin. Although the cell viability slightly decreased (175.5 ± 18.7%–121.88 ± 19.1%) with increasing β-CD content, as excessive CDs may cause disturbances of cell membranes [64]. Yet, the results demonstrated better biocompatibility than the control group. Therefore, all samples $P_5C_{Z\text{-}H}GC_{10}$-Cur possessed a

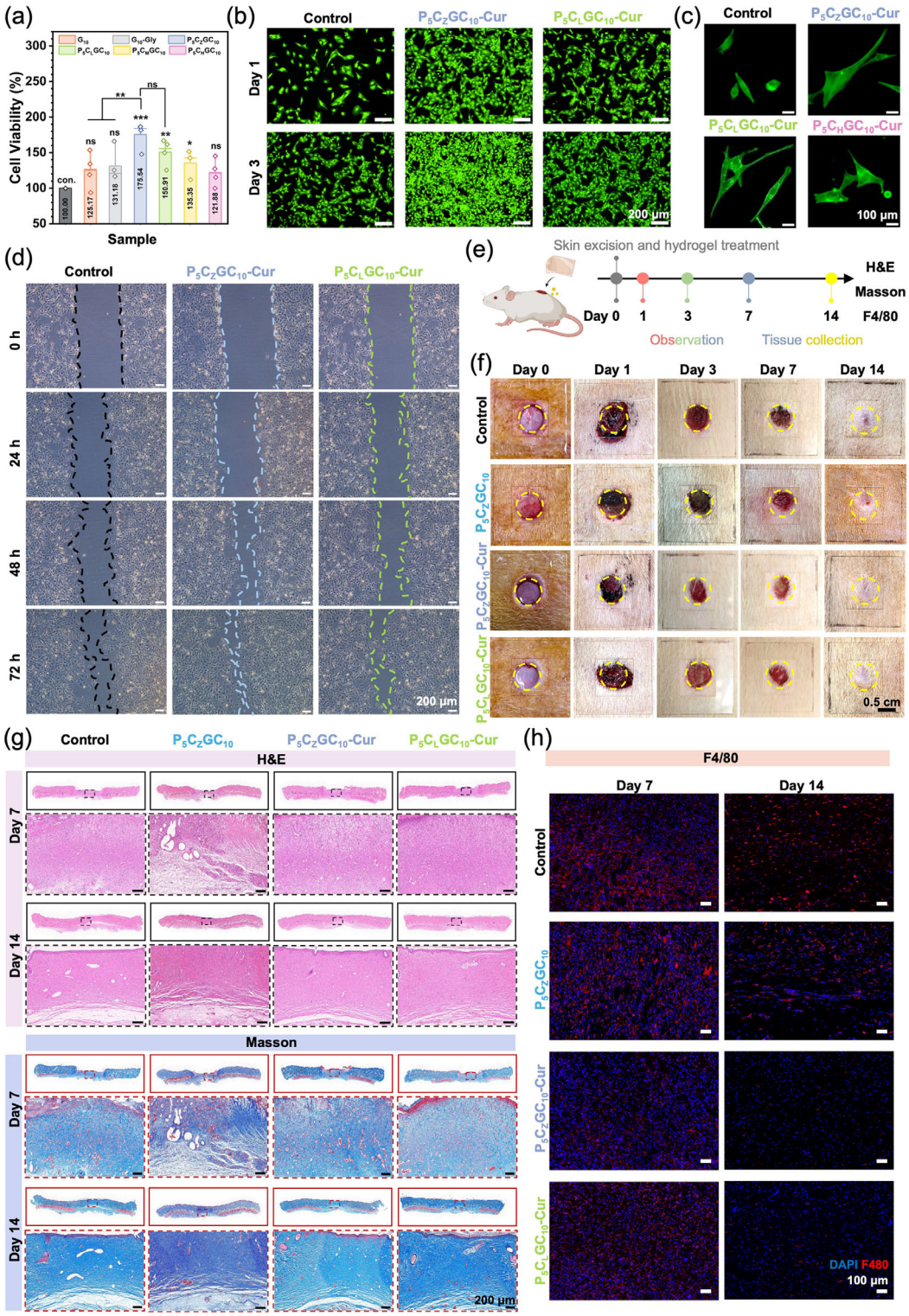

FIGURE 6 | Cytocompatibility and in vivo wound healing effects of hydrogels. (a) Cell viability of NIH/3T3 cells after being treated with extracts of G_{10}-Cur, G_{10}-Gly-Cur and $P_5C_{Z\text{-}H}GC_{10}$-Cur for 24 h. Data are presented as mean ± SD; $^*p < 0.05$, $^{**}p < 0.01$, $^{***}p < 0.001$, and ns denotes non-significant difference. $n \geq 3$. (b) Live/dead staining of NIH/3T3 cells after being treated with $P_5C_{Z\text{-}L}GC_{10}$-Cur for 1 day and 3 days. Scale bar: 200 μm. (c) Representative images of Phalloidin staining of F-actin in NIH/3T3 cells cultured on the tissue culture plate (Control) and various hydrogels $P_5C_ZGC_{10}$-Cur (50.16 kPa), $P_5C_LGC_{10}$-Cur (67.12 kPa), $P_5C_HGC_{10}$-Cur (250.68 kPa). Scale bars: 100 μm. (d) Representative images of the scratch area of NIH/3T3 cells after being treated with $P_5C_{Z\text{-}L}GC_{10}$-Cur for 3 days. Scale bar: 200 μm. (e) Schematic diagram of the healing experiment of wounds. $n = 6$. (f) Representative photographs of wounds in rats treated with PBS, $P_5C_ZGC_{10}$, $P_5C_{Z\text{-}L}GC_{10}$-Cur hydrogels on days 0, 1, 3, 7, and 14. Scale bar: 0.5 cm. (g) Histological images of H&E staining and Masson trichrome staining of wounds at days 7 and 14 for each treatment group. Scale bar: 200 μm. (h) Immunohistochemistry of control and hydrogels $P_5C_ZGC_{10}$, $P_5C_{Z\text{-}L}GC_{10}$-Cur treated wounds on day 7 and 14, stained for F4/80. F4/80-positive cells (red fluorescence) identified the infiltration of macrophages. Scale bar: 100 μm.

broad safety window and excellent cytocompatibility for TE applications.

Based on the mechanical analysis, $P_5C_{Z\text{-}L}GC_{10}$-Cur was considered a promising candidate for skin wound dressings due to its elastic, reciprocating, and low-dissipating properties. To further investigate the actual functionality of these hydrogels, $P_5C_{Z\text{-}L}GC_{10}$-Cur samples were further explored through live/dead cell staining, cell migration, and in vivo wound healing. Figure 6b shows that most cells were alive and spaced regularly with spindle-like morphology and significantly proliferated from day 1 to day 3. In addition, the adaptability of cells to matrix mechanics was reflected by corresponding alterations in actin cytoskeleton arrangement [65]. It was previously reported that NIH/3T3 cells had no detectable stress fibers on soft gels (e.g., 180 and 1600 Pa), with a slower growth rate than on a stiffer gel (55 kPa) [66]. Here, the morphology and spreading behavior of NIH/3T3 cells were visualized via F-actin staining after being plated on four substrates: tissue culture plate (Control), $P_5C_ZGC_{10}$-Cur (50.16 kPa), $P_5C_LGC_{10}$-Cur (67.12 kPa) and $P_5C_HGC_{10}$-Cur (250.68 kPa) (Figure 6c). NIH/3T3 cultured on hydrogel $P_5C_{Z\text{-}L}GC_{10}$-Cur, which resembled a stiffness close to dermal tissues (12–60 kPa) [51], showed spreading and an elongated shape with well-organized stress fibers. The cells on $P_5C_HGC_{10}$-Cur exhibited a more rounded shape and poor actin filaments, due to mechanical mismatch. Quantitative analysis (Figure S22) confirmed that the cells on $P_5C_ZGC_{10}$-Cur achieved the highest spreading area and polarization, significantly better than the harder $P_5C_HGC_{10}$-Cur variant. In the migration test (Figure 6d), the scratch area decreased over time for all groups. According to semi-quantitative analysis (Figure S23), the extractions of $P_5C_ZGC_{10}$-Cur could promote the migration of fibroblasts more effectively (80.98 ± 7.69%).

The in vivo wound healing effect of hydrogels was evaluated by a rat skin full-thickness skin defect model. A circular holodermal wound (8 mm in diameter) was created on the back skin of rats, and either left untreated (control) or treated with $P_5C_ZGC_{10}$, $P_5C_ZGC_{10}$-Cur, and $P_5C_LGC_{10}$-Cur (Figure 6e,f). The inclusion of the curcumin-free $P_5C_ZGC_{10}$ group served to distinguish the contributions of the hydrogel's mechanical cues from the pharmacological effects of curcumin. On Day 1, the astringent effects of the $P_5C_ZGC_{10}$-Cur group began to be evident and became more pronounced in the following days. By Day 7, obvious scabs were observed in the control group. Interestingly, the drug-free $P_5C_ZGC_{10}$ promoted wound closure as well compared to the control, confirming that the hydrogel matrix itself provides a favorable moist microenvironment and structural support for tissue repair. Whereas $P_5C_{Z\text{-}L}GC_{10}$-Cur significantly avoided scarring and accelerated wound healing due to the synergistic contribution of the anti-inflammatory and antibacterial properties of curcumin [56]. By day 14, quantitative analysis (Figure S24) revealed clear differences between groups across all pairwise comparisons, where the wounds in the $P_5C_ZGC_{10}$-Cur groups were almost completely closed (95.36 ± 0.84%), demonstrating good therapeutic efficacy.

Histological analysis was carried out to gain further insight into the healing status of skin wounds. The H&E staining and Masson staining results of the tissue sections are shown in Figure 6g, along with an immunofluorescence staining of F4/80 for marking the infiltration of macrophages (Figure 6h). On day 7, all groups were in the transitional stage from inflammation to proliferation. However, the control group still showed significant inflammatory cell infiltration and sparse collagen accumulation with fine fibers and low mechanical strength. This was also the reason for the appearance of scabs on the wound surface (Figure 6f), as inflammation and disorderly collagen deposition would lead to scar formation [67]. According to quantification of inflammatory cells and collagen fibers on day 7 (Figure S25), the $P_5C_ZGC_{10}$-Cur groups exhibited the best performance of an attenuated inflammatory response (11.12 ± 0.21%) and enhanced collagen deposition (67.89 ± 4.28%), compared to the control and Cur-free $P_5C_ZGC_{10}$ group, demonstrating guidance for early wound repair. Corresponding results were also shown in F4/80 immunofluorescence staining (Figure 6h), with a high density of F4/80 positive cells (red fluorescence) in the control and Cur-free $P_5C_ZGC_{10}$ group, which indicated a strong inflammatory response. The signal of infiltrating macrophages was significantly attenuated in the $P_5C_ZGC_{10}$-Cur group, suggesting its regulatory effect on inflammation. Then, on day 14, all wounds in each group had basically completed re-epithelialization. The control group had a relatively thin epidermal layer, loose and disordered collagen fibers in the dermis layer, as well as the persistence of residual inflammatory cells. The drug-free $P_5C_ZGC_{10}$ group outperformed the control slightly, suggesting that the mechanical cues of the hydrogel alone effectively guided tissue remodeling. Conversely, the wounds of $P_5C_{Z\text{-}L}GC_{10}$-Cur samples were more mature, with more granulation tissue replaced and accompanied by regeneration of skin appendages. Especially in the $P_5C_ZGC_{10}$-Cur sample, the inflammatory signal nearly vanished, and collagen fiber bundles became thicker and highly organized, which even surrounded newly formed appendages, exhibiting a promising tissue regeneration effect. Therefore, collectively in vitro and in vivo, both $P_5C_{Z\text{-}L}GC_{10}$-Cur effectively promoted wound healing. A better performance of $P_5C_ZGC_{10}$-Cur is likely related to a more suitable β-CD content and mechanical cues that are more compatible with fibroblasts at the wound site.

3 | Conclusion

In summary, we have prepared a series of hydrogels based on PEGDA-β-CD polyrotaxane and gelatin derivative in glycerol/water binary solution with tunable mechanical properties by adjusting the threading density of polyrotaxane, enabling the design on-demand in tissue engineering. A PEGDA-β-CD polypseudorotaxane, formed via host–guest recognition, was first captured in a low-concentration aqueous environment. Meanwhile, the results demonstrated that the threading density at the molecular level guided the evolution of the hydrogel's microstructure and further transmitted to macroscopic mechanical properties. The introduction of a PEGDA-β-CD polyrotaxane structure enhanced the toughness and elastic modulus of gels, allowing customization to tissues or organs with different stiffness. In addition, the gel with high threading density of β-CD enabled a dynamic bond motif with a sliding-ring effect during stretching. The final four formulations of hydrogels $P_5C_{Z\text{-}H}GC_{10}$-Cur exhibited different directions of usage in TE: $P_5C_{Z\text{-}L}GC_{10}$-Cur, characterized by highly elastic, recoverable, and low dissipation materials, was suitable for joint skin dressings, while $P_5C_{M\text{-}H}GC_{10}$-Cur preferred to mimic special biological tissues with high modulus and high damping properties. All

samples exhibited excellent biocompatibility, and $P_5C_ZGC_{10}$-Cur featured the best wound healing effects with fibroblasts NIH/3T3 proliferation and migration, anti-inflammation, and promotion of collagen accumulation. Overall, this study established not only a clear structure-property-function relationship across molecular, microscale, and macroscale levels but also the critical role of polyrotaxane threading density in governing mechanical adaptability and biological performance. This strategy provides general design principles for mechanically programmable supramolecular biomaterials and opens new avenues for engineering dynamic tissue-mimetic systems.

Author Contributions

S.Y.C. and P.T. conceived this idea and managed the research. S.Y.C. designed and prepared hydrogels $P_5C_{Z\text{-}H}GC_{10}$ and planned all subsequent tests. S.Y.C. and X.D.X. designed the in vitro cell tests and in vivo animal experiments, and X.D.X. performed all of them. H.P.S. and S.Y.C. validated the structure of polyrotaxane PEGDA-β-CD. D.V. and S.Y.C. conducted observations on the microstructure. X.H.X. provided guidance in rheological testing. S.Y.C. and X.D.X. drafted the manuscript. H.P.S., D.V., J.F.W., T.T.C., C.W.S., S.B., P.L., P.T. revised the manuscript. The manuscript was written with contributions from all authors. All authors have given their approval to the final version of the manuscript.

Acknowledgements

S. Chen acknowledges financial support from the China Scholarship Council (CSC, file No. 202408080035). P. Théato acknowledges funding from the Helmholtz Association (43.33.11). Financial support from the Karlsruhe Institute of Technology (KIT) is deeply appreciated. S. Chen acknowledges the research group of Prof. Dr. Manfred Wilhelm (ITCP, KIT) for sharing equipment during this work and Ingrid Zeller from AK Wilhelm for her support in SEM testing.

Open access funding enabled and organized by Projekt DEAL.

Funding

This study was financially supported by the China Scholarship Council (CSC, No. 202408080035) and the Helmholtz Association (43.33.11).

Ethics Statement

Animal procedures were authorized by the Medical Ethics Committee of Sichuan Provincial People's Hospital (Approval No. 2025381) and conducted in accordance with the university's Guidelines for Care and Use of Laboratory Animals.

Conflicts of Interest

The authors declare no conflicts of interest.

Data Availability Statement

The data and movies that support the findings of this study are available in the Supporting Information of this article. The raw data of the manuscript and the Supporting Information are publicly available in the RADAR4ChemRepository under the following https://doi.org/10.22000/2y2deb4v7sv6p1df.

References

1. M. Nayak, D. Banerjee, V. Venugopal, S. K. Nethi, A. K. Barui, and S. Mukherjee, "Cell-Engineered Technologies for Wound Healing and Tissue Regeneration," *Npj Biomedical Innovations* 2, no. 1 (2025): 38, https://doi.org/10.1038/s44385-025-00042-w.

2. P. Bertsch, M. Diba, D. J. Mooney, and S. C. G. Leeuwenburgh, "Self-Healing Injectable Hydrogels for Tissue Regeneration," *Chemical Reviews* 123, no. 2 (2023): 834–873, https://doi.org/10.1021/acs.chemrev.2c00179.

3. M. U. A. Khan, G. M. Stojanovic, M. F. B. Abdullah, et al., "Fundamental Properties of Smart Hydrogels for Tissue Engineering Applications: A Review," *International Journal of Biological Macromolecules* 254 (2024): 127882, https://doi.org/10.1016/j.ijbiomac.2023.127882.

4. U. Blache, E. M. Ford, B. Ha, et al., "Engineered Hydrogels for Mechanobiology," *Nature Reviews Methods Primers* 2, no. 1 (2022): 98, https://doi.org/10.1038/s43586-022-00179-7.

5. K. Y. Lee and D. J. Mooney, "Hydrogels for Tissue Engineering," *Chemical Reviews* 101, no. 7 (2001): 1869–1880, https://doi.org/10.1021/cr000108x.

6. D. E. Discher, P. Janmey, and Y. Wang, "Tissue Cells Feel and Respond to the Stiffness of Their Substrate," *Science* 310, no. 5751 (2005): 1139–1143, https://doi.org/10.1126/science.1116995.

7. S. Scott, M. Villiou, F. Colombo, et al., "Dynamic and Reversible Tuning of Hydrogel Viscoelasticity by Transient Polymer Interactions for Controlling Cell Adhesion," *Advanced Materials* 37, no. 12 (2025): 2408616, https://doi.org/10.1002/adma.202408616.

8. Y. Kalukula, G. Ciccone, D. Mohammed, et al., "Unlocking the Therapeutic Potential of Cellular Mechanobiology," *Science Advances* 11, no. 44 (2025): aea6817, https://doi.org/10.1126/sciadv.aea6817.

9. J. P. Gong, Y. Katsuyama, T. Kurokawa, and Y. Osada, "Double-Network Hydrogels with Extremely High Mechanical Strength," *Advanced Materials* 15, no. 14 (2003): 1155–1158, https://doi.org/10.1002/adma.200304907.

10. D. Zhong, Z. Wang, J. Xu, et al., "A Strategy for Tough and Fatigue-Resistant Hydrogels via Loose Cross-Linking and Dense Dehydration-Induced Entanglements," *Nature Communications* 15, no. 1 (2024): 5896, https://doi.org/10.1038/s41467-024-50364-3.

11. X. Xiong, Y. Chen, Z. Wang, et al., "Polymerizable Rotaxane Hydrogels for Three-Dimensional Printing Fabrication of Wearable Sensors," *Nature Communications* 14, no. 1 (2023): 1331, https://doi.org/10.1038/s41467-023-36920-3.

12. T. Higashi, T. Taharabaru, and K. Motoyama, "Synthesis of Cyclodextrin-Based Polyrotaxanes and Polycatenanes for Supramolecular Pharmaceutical Sciences," *Carbohydrate Polymers* 337 (2024): 122143, https://doi.org/10.1016/j.carbpol.2024.122143.

13. L. Chen, X. Sheng, G. Li, and F. Huang, "Mechanically Interlocked Polymers Based on Rotaxanes," *Chemical Society Reviews* 51, no. 16 (2022): 7046–7065, https://doi.org/10.1039/d2cs00202g.

14. C. Zhang, Y. Shen, M. Huang, et al., "Dynamic Hydrogel Mechanics in Organoid Engineering: From Matrix Design to Translational Paradigms," *Bioactive Materials* 55 (2026): 144–170, https://doi.org/10.1016/j.bioactmat.2025.09.021.

15. Z.-M. Lv, Y.-Y. Liu, S.-B. Yu, J. Tian, Y.-X. Xu, and Z.-T. Li, "Polyrotaxanes in Motion: Recent Advances in Slide-Ring Supramolecular Polymers," *Supramolecular Materials* 5 (2026): 100114, https://doi.org/10.1016/j.supmat.2025.100114.

16. J. Wankar, N. G. Kotla, S. Gera, S. Rasala, A. Pandit, and Y. A. Rochev, "Recent Advances in Host–Guest Self-Assembled Cyclodextrin Carriers: Implications for Responsive Drug Delivery and Biomedical Engineering," *Advanced Functional Materials* 30, no. 44 (2020): 1909049, https://doi.org/10.1002/adfm.201909049.

17. A. Harada, J. Li, and M. Kamachi, "The Molecular Necklace: A Rotaxane Containing Many Threaded α-Cyclodextrins," *Nature* 356, no. 6367 (1992): 325–327, https://doi.org/10.1038/356325a0.

18. K. A. Udachin, L. D. Wilson, and J. A. Ripmeester, "Solid Polyrotaxanes of Polyethylene Glycol and Cyclodextrins: the Single Crystal X-Ray Structure of PEG–β-Cyclodextrin," *Journal of the American Chemical Society* 122, no. 49 (2000): 12375–12376, https://doi.org/10.1021/ja002189k.

19. J. Zheng, Z. Yang, Y. Sang, F. Zhang, Y. Zhang, and P. Zhang, "A Simple Preparation Method of Rotaxane Cross-Linker Based on γ-

Cyclodextrin and Its Application in Hydrogel Materials," *Materials Today Communications* 33 (2022): 104760, https://doi.org/10.1016/j.mtcomm.2022.104760.

20. G. Kali, S. Haddadzadegan, and A. Bernkop-Schnürch, "Cyclodextrins and Derivatives in Drug Delivery: New Developments, Relevant Clinical Trials, and Advanced Products," *Carbohydrate Polymers* 324 (2024): 121500, https://doi.org/10.1016/j.carbpol.2023.121500.

21. R. Challa, A. Ahuja, J. Ali, and R. K. Khar, "Cyclodextrins in Drug Delivery: An Updated Review," *Aaps Pharmscitech [Electronic Resource]* 6, no. 2 (2005): E329–E357, https://doi.org/10.1208/pt060243.

22. Y. Akae, "Cyclodextrin-Based Rotaxanes for Polymer Materials: Challenge on Simultaneous Realization of Inexpensive Production and Defined Structures," *Beilstein Journal of Organic Chemistry* 20, no. 1 (2024): 3026–3049, https://doi.org/10.3762/bjoc.20.252.

23. C. Capacchione, P. Della Sala, I. Quaratesi, et al., "Poly(Ethylene Glycol)/β-Cyclodextrin Pseudorotaxane Complexes as Sustainable Dispersing and Retarding Materials in a Cement-Based Mortar," *ACS Omega* 6, no. 18 (2021): 12250–12260, https://doi.org/10.1021/acsomega.1c01133.

24. M. Hayduk, T. Schaller, F. C. Niemeyer, et al., "Phosphorescence Induction by Host-Guest Complexation with Cyclodextrins – The Role of Regioisomerism and Affinity," *Chemistry – A European Journal* 28, no. 51 (2022): 202201081, https://doi.org/10.1002/chem.202201081.

25. M. Haouas, C. Falaise, N. Leclerc, S. Floquet, and E. Cadot, "NMR Spectroscopy to Study Cyclodextrin-Based Host–guest Assemblies with Polynuclear Clusters," *Dalton Transactions* 52, no. 38 (2023): 13467–13481, https://doi.org/10.1039/D3DT02367B.

26. H. Xu, T. K. Ronson, A. W. Heard, et al., "A Pseudo-Cubic Metal–Organic Cage with Conformationally Switchable Faces for Dynamically Adaptive Guest Encapsulation," *Nature Chemistry* 17, no. 2 (2025): 289–296, https://doi.org/10.1038/s41557-024-01708-5.

27. J. Wan, S. Xu, J. Li, et al., "Facile Synthesis of Multifunctional Pharmaceutical Carbon Dots for Targeted Bioimaging and Chemotherapy of Tumors," *Nanoscale* 14, no. 31 (2022): 11359–11368, https://doi.org/10.1039/D2NR03321F.

28. J. Li, J. Tong, X. Li, Z. Yang, Y. Zhang, and G. Diao, "Facile Microfluidic Synthesis of Copolymer Hydrogel Beads for the Removal of Heavy Metal Ions," *Journal of Materials Science* 51, no. 23 (2016): 10375–10385, https://doi.org/10.1007/s10853-016-0258-0.

29. M. Tajbakhsh and M. R. Naimi-Jamal, "Copper-Doped Functionalized β-Cyclodextrin as an Efficient Green Nanocatalyst for Synthesis of 1,2,3-Triazoles in Water," *Scientific Reports* 12, no. 1 (2022): 4948, https://doi.org/10.1038/s41598-022-08868-9.

30. L. Szente, J. Szemán, and T. Sohajda, "Analytical Characterization of Cyclodextrins: History, Official Methods and Recommended New Techniques," *Journal of Pharmaceutical and Biomedical Analysis* 130 (2016): 347–365, https://doi.org/10.1016/j.jpba.2016.05.009.

31. U. Conway, A. D. Warren, C. J. Arthur, and P. J. Gates, "A Study of the Application of Graphite MALDI to the Analysis of Short-Chain Polyethylene Glycols," *Polymer Chemistry* 12, no. 3 (2021): 439–448, https://doi.org/10.1039/D0PY01493A.

32. K. D. Trotter, O. Owojaiye, S. P. Meredith, et al., "The Interaction of Silver(II) Complexes with Biological Macromolecules and Antioxidants," *Biometals* 32, no. 4 (2019): 627–640, https://doi.org/10.1007/s10534-019-00198-0.

33. X. Zhou, Z. Luo, A. Baidya, et al., "Biodegradable β -Cyclodextrin Conjugated Gelatin Methacryloyl Microneedle for Delivery of Water-Insoluble Drug," *Advanced Healthcare Materials* 9, no. 11 (2020): 2000527, https://doi.org/10.1002/adhm.202000527.

34. F. Chen, Y. Shen, Y. Shao, et al., "Functional Hydrogel for Modulating Lipid Droplets and Neuroinflammation in Head Injury," *Advanced Functional Materials* 35, no. 52 (2025): 07086, https://doi.org/10.1002/adfm.202507086.

35. J. Wan, X. Zhang, Y. Jiang, et al., "Regulation of Multi-Color Fluorescence of Carbonized Polymer Dots by Multiple Contributions of Effective Conjugate Size, Surface state, and Molecular Fluorescence," *Journal of Materials Chemistry B* 10, no. 36 (2022): 6991–7002, https://doi.org/10.1039/D2TB01330D.

36. S. Chen, N. Hassan, A. Kopp, et al., "Theragenerative Injectable Bone-Adhesive Hydrogels for Combined Photothermal Osteosarcoma Therapy and Bone Repair," *Biomaterials Science* 13 (2025): 3544–3560, https://doi.org/10.1039/D5BM00559K.

37. N. Emara, "Antibacterial Activity of Magnetic Nanoparticles Synthesized from Recycling of Steel Industry Wastes," *International Journal of Engineering Science* 6 (2015): 8640–8648.

38. M. Karimi, M. Mashreghi, S. S. Saremi, and M. R. Jaafari, "Spectrofluorometric Method Development and Validation for the Determination of Curcumin in Nanoliposomes and Plasma," *Journal of Fluorescence* 30, no. 5 (2020): 1113–1119, https://doi.org/10.1007/s10895-020-02574-3.

39. A. Bergal and M. Andac, "Detailed Investigation and Influence of Oxidation Degree on Synthesis, Characterization and Antibacterial Activity of β- cyclodextrin," *Carbohydrate Research* 533 (2023): 108936, https://doi.org/10.1016/j.carres.2023.108936.

40. A. Roy, S. Zenker, S. Jain, et al., "A Highly Stretchable, Conductive, and Transparent Bioadhesive Hydrogel as a Flexible Sensor for Enhanced Real-Time Human Health Monitoring," *Advanced Materials* 36, no. 35 (2024): 2404225, https://doi.org/10.1002/adma.202404225.

41. B. Li, "Surface Wrinkling Patterns on a Core-Shell Soft Sphere," *Physical Review Letters* 106, no. 23 (2011): 234301, https://doi.org/10.1103/PhysRevLett.106.234301.

42. M. Kato, Y. Kashihara, T.-A. Asoh, and H. Uyama, "Geometry Control of Wrinkle Structures Aligned on Hydrogel Surfaces," *Langmuir* 36, no. 6 (2020): 1467–1473, https://doi.org/10.1021/acs.langmuir.9b03967.

43. C. Kassapoglou, "Determination of Energy Dissipation during Cyclic Loading and Its Use to Predict Fatigue Life of Metal Alloys," *Fatigue & Fracture of Engineering Materials & Structures* 46, no. 10 (2023): 3667–3679, https://doi.org/10.1111/ffe.14096.

44. Q. Zhang, H. Xu, C. Wu, et al., "Tissue Fluid Triggered Enzyme Polymerization for Ultrafast Gelation and Cartilage Repair," *Angewandte Chemie International Edition* 60, no. 36 (2021): 19982–19987, https://doi.org/10.1002/anie.202107789.

45. J. Diani, B. Fayolle, and P. Gilormini, "A Review on the Mullins Effect," *European Polymer Journal* 45, no. 3 (2009): 601–612, https://doi.org/10.1016/j.eurpolymj.2008.11.017.

46. M. Li, Y. Lin, Y. Zhang, L. Bian, and K. Zhang, "Energy-Dissipative Hydrogels: A Promising Material for Tissue Regeneration †," *Chinese Journal of Chemistry* 41, no. 20 (2023): 2697–2714, https://doi.org/10.1002/cjoc.202300167.

47. K. Chen, Z. Wu, Y. Liu, Y. Yuan, and C. Liu, "Injectable Double-Crosslinked Adhesive Hydrogels with High Mechanical Resilience and Effective Energy Dissipation for Joint Wound Treatment," *Advanced Functional Materials* 32 (2022): 2109687, https://doi.org/10.1002/adfm.202109687.

48. Z. Zhuang, C. Gu, S. Li, et al., "Materials and Structures Inspired by Human Heel Pads for Advanced Biomechanical Function," *Biomimetics* 10, no. 5 (2025): 267, https://doi.org/10.3390/biomimetics10050267.

49. Z. Liu, G. Liang, Y. Zhan, et al., "A Soft yet Device-Level Dynamically Super-Tough Supercapacitor Enabled by an Energy-Dissipative Dual-Crosslinked Hydrogel Electrolyte," *Nano Energy* 58 (2019): 732–742, https://doi.org/10.1016/j.nanoen.2019.01.087.

50. Q. Zhou, S. Zhou, D. Puglia, et al., "Ultrastretchable and Recyclable Ionogels with Hierarchical Dynamic Bonds for Respiratory Monitoring," *Advanced Functional Materials* 36, no. 2 (2026): 12398, https://doi.org/10.1002/adfm.202512398.

51. C.-H. Kuan, Y.-N. Wang, E.-F. Liao, et al., "Viscoelastic Hydrogel with Mechanomodulatory Tension Shielding and Time-Dependent

Immunomodulatory Effects for Scarless Healing," *Advanced Healthcare Materials* 14, no. 32 (2025): 01954, https://doi.org/10.1002/adhm.202501954.

52. A. Santos and D. Lagares, "Matrix Stiffness: The Conductor of Organ Fibrosis," *Current Rheumatology Reports* 20, no. 1 (2018): 2, https://doi.org/10.1007/s11926-018-0710-z.

53. Y. Liang, J. He, and B. Guo, "Functional Hydrogels as Wound Dressing to Enhance Wound Healing," *ACS Nano* 15, no. 8 (2021): 12687–12722, https://doi.org/10.1021/acsnano.1c04206.

54. R. Teshima, S. Osawa, M. Yoshikawa, Y. Kawano, H. Otsuka, and T. Hanawa, "Low-Adhesion and Low-Swelling Hydrogel Based on Alginate and Carbonated Water to Prevent Temporary Dilation of Wound Sites," *International Journal of Biological Macromolecules* 254 (2024): 127928, https://doi.org/10.1016/j.ijbiomac.2023.127928.

55. Y. Okumura and K. Ito, "The Polyrotaxane Gel: A Topological Gel by Figure-Of-Eight Cross-Links," *Advanced Materials* 13, no. 7 (2001): 485–487, https://doi.org/10.1002/1521-4095(200104)13:7%3C485::AID-ADMA485%3E3.0.CO;2-T.

56. Z. Fu, J. Zou, J. Zhong, et al., "Curcumin-Loaded Nanocomposite Hydrogel Dressings for Promoting Infected Wound Healing and Tissue Regeneration," *International Journal of Nanomedicine* 19 (2024): 10479–10496, https://doi.org/10.2147/IJN.S479330.

57. H. Wang, L. Hao, P. Wang, M. Chen, S. Jiang, and S. Jiang, "Release Kinetics and Antibacterial Activity of Curcumin Loaded Zein Fibers," *Food Hydrocolloids* 63 (2017): 437–446, https://doi.org/10.1016/j.foodhyd.2016.09.028.

58. A. Aizaz, M. H. Nawaz, M. S. Ismat, et al., "Development and Characterization of Polyethylene Oxide and Guar Gum-Based Hydrogel; a Detailed in-Vitro Analysis of Degradation and Drug Release Kinetics," *International Journal of Biological Macromolecules* 273 (2024): 132824, https://doi.org/10.1016/j.ijbiomac.2024.132824.

59. N. Al-Jawuschi, S. Chen, N. Abie, T. Fischer, S. Fare, and H. H. Maleki, "Self-Assembly-Driven Bi_2S_3 Nanobelts Integrated a Silk-Fibroin-Based 3D-Printed Aerogel-Based Scaffold with a Dual-Network Structure for Photothermal Bone Cancer Therapy," *Langmuir* 39, no. 12 (2023): 4326–4337, https://doi.org/10.1021/acs.langmuir.2c03334.

60. F. Yang, Y. Xue, F. Wang, et al., "Sustained Release of Magnesium and Zinc Ions Synergistically Accelerates Wound Healing," *Bioactive Materials* 26 (2023): 88–101, https://doi.org/10.1016/j.bioactmat.2023.02.019.

61. X. Zhao, Q. Lang, L. Yildirimer, et al., "Photocrosslinkable Gelatin Hydrogel for Epidermal Tissue Engineering," *Advanced Healthcare Materials* 5, no. 1 (2016): 108–118, https://doi.org/10.1002/adhm.201500005.

62. Y. Piao, H. You, T. Xu, et al., "Biomedical Applications of Gelatin Methacryloyl Hydrogels," *Engineered Regeneration* 2 (2021): 47–56, https://doi.org/10.1016/j.engreg.2021.03.002.

63. K. Su and C. Wang, "Recent Advances in the Use of Gelatin in Biomedical Research," *Biotechnology Letters* 37, no. 11 (2015): 2139–2145, https://doi.org/10.1007/s10529-015-1907-0.

64. F. Leroy-Lechat, D. Wouessidjewe, J.-P. Andreux, F. Puisieux, and D. Duchêne, "Evaluation of the Cytotoxicity of Cyclodextrins and Hydroxypropylated Derivatives," *International Journal of Pharmaceutics* 101, no. 1 (1994): 97–103, https://doi.org/10.1016/0378-5173(94)90080-9.

65. Y. Chen, L. Wang, H. Huang, et al., "Mechano-Regulatory Cellular Behaviors of NIH/3T3 in Response to the Storage Modulus of Liquid Crystalline Substrates," *Journal of the Mechanical Behavior of Biomedical Materials* 57 (2016): 42–54, https://doi.org/10.1016/j.jmbbm.2015.11.005.

66. T. Yeung, P. C. Georges, L. A. Flanagan, et al., "Effects of Substrate Stiffness on Cell Morphology, Cytoskeletal Structure, and Adhesion," *Cell Motility and the Cytoskeleton* 60, no. 1 (2005): 24–34, https://doi.org/10.1002/cm.20041.

67. M. Xue and C. J. Jackson, "Extracellular Matrix Reorganization during Wound Healing and Its Impact on Abnormal Scarring," *Advances in Wound Care* 4, no. 3 (2015): 119–136, https://doi.org/10.1089/wound.2013.0485.

Supporting Information

Additional supporting information can be found online in the Supporting Information section.

Supporting File 1: adfm77853-sup-0001-SuppMat.docx.

Supporting File 2: adfm77853-sup-0002-MovieS1.mov.

Supporting File 3: adfm77853-sup-0003-MovieS2.MOV.